Calibration and Direction-of-Arrival Estimation of mm-Wave Radars: A Practical Introduction

Claudia Vasanelli, Fabian Roos, André Dürr, Johannes Schlichenmaier, Philipp Hügler, Benedikt Meinecke, Maximilian Steiner, and Christian Waldschmidt

Calibration and Direction-of-Arrival Estimation of mm-Wave Radars: A Practical Introduction

Claudia Vasanelli, *Student Member, IEEE,* Fabian Roos, *Student Member, IEEE,* André Dürr, *Student Member, IEEE,* Johannes Schlichenmaier, *Student Member, IEEE,* Philipp Hügler, *Student Member, IEEE,* Benedikt Meinecke, *Student Member, IEEE,* Maximilian Steiner, *Student Member, IEEE,* Christian Waldschmidt, *Senior Member, IEEE*

Abstract—Have you read everything about direction-of-arrival estimation in textbooks but are you still uncertain how to realize it in practice? This tutorial-like paper will help to link the theory with a practical approach for direction-of-arrival estimation using mm-wave radar systems and it deals with arising challenges. Step by step, it is explained how to move from the measured time domain data to the estimated angular position of the target. Since the target angle estimation is usually carried out after range-velocity processing, the required pre-processing steps are described. The assessment criteria to form the relationship between array design and radar performance are expressed with the Rayleigh criterion for angular resolution and the ambiguity function as a measure for the unambiguous angular range. An in-depth instruction on how to carry out the sensor calibration is provided. Besides the choice of a proper calibration object, the required number of measurements and signal-to-noise ratio related issues are considered and supported by measurement results. The discussion of single- and multi-target measurements with the calibrated sensor concludes this work.

I. MOTIVATION

In the last decade, mm-wave radars gained a strong interest in the scientific community. The huge advancements in the semiconductor technology and the cost-effective development of monolithic microwave integrated circuits (MMIC) for the generation of the high-frequency signal allowed the mass production of radar transceivers. In particular, nowadays mm-wave radar sensors are well-established as key sensor technology for many automotive [1], [2], civil [3], [4], and industrial [5], [6] applications. At the present time it is even possible to simply buy state-of-the-art off-the-shelf radar platforms for research, educational purposes, or rapid testing [7], [8]. The plug-and-play era of mm-wave radars seems just getting started.

Millimeter-wave radars are able to provide precise distance and velocity measurements even in poor visibility or harsh environmental conditions, where the performance of other sensor technologies starts to decrease [1]. Moreover, thanks to the short wavelength they show appealing compact dimensions.

In addition to range and velocity, mm-wave radar sensors typically employ more than one receiving channel to get also the angular position of the target.

In most of the applications, the estimation of the angular position of the target, i.e., direction-of-arrival estimation (DoA), is performed with digital beamforming on the receiver side, since the use of mechanical scanning or phased array systems is too expensive. In particular, the target angle estimation is

carried out usually after the range-velocity processing, and it is necessary to separate targets that share the same range-velocity bin. Thus, the DoA estimation is rather independent of the radar waveform and modulation scheme, while it is strictly related to the properties of the receiving antenna array.

In the last years the use of multiple-input multiple-output (MIMO) radars became a popular solution to increase the angular resolution of the radar sensor, thanks to the larger virtual aperture that extends the physical aperture of the receiving array. Some examples of mm-wave MIMO radars can be found in [9], [10], and [11].

Processing the signal received by a (virtual) receiving array of antennas for the purpose of angle measurements is a well-established topic in both the antenna and signal processing communities [12]. A number of different approaches have been developed over the last decades; some of them have been summarized for example by [12] and [13]. However, the antenna engineer that tackles for the first time the array processing with the help of state-of-the-art mm-wave radars could feel overwhelmed while approaching as a newbie a DoA estimation problem. A number of practical questions might come to mind that can rarely be quickly answered by most of the scientific literature.

This paper guides the reader towards an efficient DoA estimation using state-of-the-art mm-wave radars. A practical approach is given. Step by step, starting from the very basic pre-processing steps, it explains how to practically perform the DoA estimation and which crucial aspects must be considered, too. For example, this paper tries to explain why the calibration of the sensor plays a significant role and how to carry it out. Moreover, some useful practical hints are given, for example to save time and processing effort during the calibration and angle estimation phases. No deep radar signal processing prior knowledge is required to follow this tutorial, and it is based on a descriptive rather than formal approach.

This paper is organized as follows. Section II presents first of all the required pre-processing steps on the measured time domain radar signal. Afterwards, the signal model is introduced in Section III. Two different simple techniques for the DoA estimation are shown, too. Section IV describes some useful criteria to assess the performance of the antenna system with regard to the DoA estimation problem. The calibration procedure and all the related challenges are reported in Section V. Some practical measurement examples are given in Section VI. Finally, the conclusions will be drawn
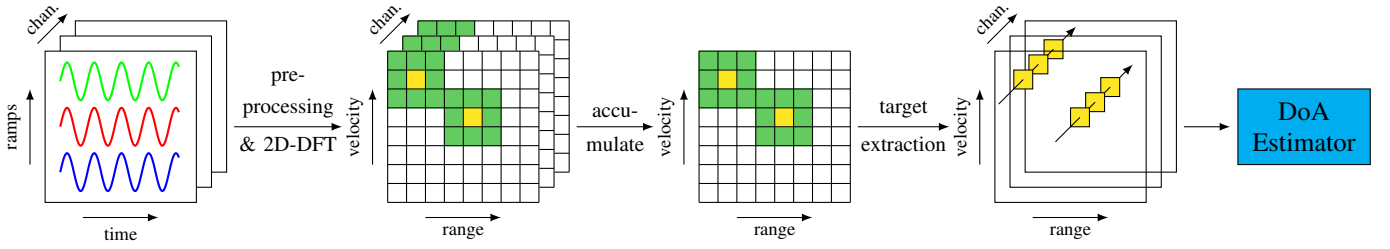
Fig. 1. Pre-processing chain for extracting the steering vectors of possible targets for a standard multi-channel radar using chirp-sequence modulation.

in Section VII.

II. PRE-PROCESSING CHAIN

The angular information of a target is present in the reflected signal in the form of the phase relations between the receiving channels. For the DoA estimation, these phase relations have to be extracted from the received radar signal.

Fig. 1 shows a conventional pre-processing chain for calculating and extracting the phase relations of possible targets with a standard multi-channel radar using the well-known chirp-sequence modulation [14], i.e., sending multiple very short frequency ramps. The targets manifest themselves as high amplitude values in certain range-velocity cells, each containing one or more target signals, that share the same range and velocity, but separate angular information.

The pre-processing chain starts with the sampled base-band beat signals in time domain for each ramp on each channel which — for a single target — manifest themselves as sinusoidal waves. These beat signals undergo — for each channel separately — a series of pre-processing steps before being converted to the range-velocity domain by means of a two-dimensional discrete Fourier transform (2D-DFT), resulting in one range-velocity matrix for each channel. The exact pre-processing steps depend on the respective scenario, but usually involve some kind of windowing function — for example a Blackman-Harris window [15] — to suppress unwanted sidelobes introduced by the DFT. Depending on the radar system architecture, additional pre-processing steps in the time domain may be performed, or zero-padding can be used to smooth out the resulting range-velocity data.

After this step, possible targets — appearing as high absolute amplitude values in specific range-velocity cells — still have to be extracted from the range-velocity matrix before feeding them into the DoA estimator. This is mostly done to reduce computational effort by discarding cells in the range-velocity domain, which most likely do not contain any targets.

For this reduction, the three-dimensional matrix from the previous steps (range-velocity-channel) first has to be accumulated into a single range-velocity matrix, which still includes information from all channels. This can be accomplished by various ways, two of them being:

- **Non-coherent integration**: Here, the phase information of the complex amplitudes in the range-velocity cells are discarded and the absolute values are summed up along the channels [16]. The advantage of this approach is that amplitudes in target cells are contributing equally throughout the channels regardless of their phase relations. The downside, however, is an increase in noise artifacts due to them not experiencing any averaging because of the missing phase.
- **Coherent integration**: By summing up the complex amplitude values of the range-velocity cells along the channels, the aforementioned downside of accumulated noise is reduced due to the random nature of the noise process. However, this also leads to the coherent summation of amplitudes for legitimate target cells. This can potentially decrease the resulting summed-up amplitude, because the values do not add up ideally due to the naturally occuring phase progression between the channels.

The accumulated matrix then provides the base for the extraction of possible target cells. This usually is accomplished by applying one or more constant false alarm rate (CFAR) algorithms to separate legitimate targets from noise and clutter. Often, an ordered statistics (OS)-CFAR algorithm, which provides good noise estimation in the presence of multiple targets and clutter edges [17], is deployed either in range, or velocity dimension, sometimes in both.

As a final extraction step, a peak search is usually performed in one or two dimensions to find the actual velocity and range of individual target points. This becomes necessary due to the non-idealities of the sampled time signals and the properties of the DFT distorting the ideal frequency peak of a signal.

With the acquired knowledge of the target cells in the range-velocity domain a cut through the non-accumulated channel matrices at their respective range-velocity positions is performed. For one target cell, this results in a vector of phase-progressing complex amplitudes describing the steering vector or — in the case of multiple targets in the same range-velocity cell — superimposed steering vectors, which subsequently is fed into the DoA estimator.

III. SIGNAL MODEL

Before going into the details of the DoA estimation, it is important to mathematically describe the steering vector obtained at the end of the pre-processing chain sketched in Fig. 1. Let M_r be the number of receivers placed in one-dimensional lattice on the x-axis as in Fig. 2. If plane waves impinge from the target, the direction of propagation of the incoming signal, namely the angle ϑ drawn in Fig. 2, is the same for each element of the array. Moreover, only the azimuth plane is of interest in this work. However, it is possible to generalize the DoA estimation towards a two-dimensional
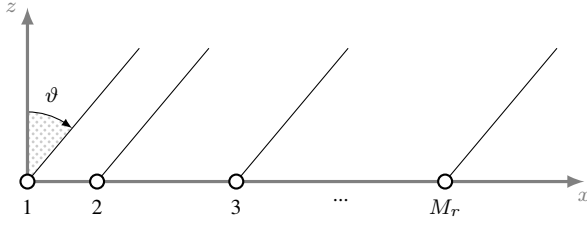
Fig. 2. Arrangement of the M_r elements of the arbitrary linear array. The angle ϑ is defined within $[-90°, 90°]$.

problem and to retrieve thus both the azimuth and elevation angles of the target. An example of a two-dimensional radar system has been given in [18].

With these assumptions it is then possible to write the steering vector of the receiving array $\boldsymbol{y}(\vartheta)$ for the angular direction ϑ as

$$\boldsymbol{y}(\vartheta) = \begin{bmatrix} e^{j2\pi \frac{x_1}{\lambda_0} \sin \vartheta} \\ \vdots \\ e^{j2\pi \frac{x_{M_r}}{\lambda_0} \sin \vartheta} \end{bmatrix}, \tag{1}$$

where λ_0 is the free-space wavelength, and x_k represents the position of the array element with $k = 1, \ldots, M_r$. If the radar sensor is a MIMO radar, then for DoA estimation purposes it is necessary to consider the steering vector associated to the virtual array, that can be calculated as the Kronecker product of the transmitting and receiving array steering vectors [19], or equivalently, by applying the vectorization to the product of transmitting and receiving array steering vectors [20]. The use of a MIMO system does not affect the calibration effort or the implementation of the angular estimation algorithm compared to the non-MIMO case. The study presented in this tutorial applies to both cases.

Finally, by considering a number of different directions of interest ϑ_i, it is possible to collect the steering vectors $\boldsymbol{y}(\vartheta_i)$ to build the steering matrix $\boldsymbol{Y}$.

A. Deterministic Maximum Likelihood Approach

This tutorial explains first of all the deterministic maximum likelihood approach (DML), where the word deterministic comes from the assumption that the received signal waveforms are deterministic and unknown [13]. The DML method becomes quite intuitive and quick to use for a single target and single snapshot scenario. Focusing on the single target case does not narrow the analysis. As shown in the previous section, the DoA estimation takes place after the range-velocity processing. It is however quite a reasonable assumption to say that only a single target occupies a range-velocity bin.

The basic idea of the DML approach is to compare the actual measurement results with a reference calibration matrix. This comparison can be mathematically calculated by means of a cross-correlation. Indeed, the direction that maximizes the cross-correlation, i.e., that returns the highest similarity, gives the estimated DoA ϑ_{est}.

The starting point for the DoA estimation is the calibration of the radar sensor to take into account the typical deviations from the ideal designed antenna system, e.g., due to fabrication

errors. Indeed, because of the small wavelength at mm-wave frequencies, the fabrication inaccuracies can potentially lead to non-negligible phase errors. This point will also be further explained in Section V. The results of the reference measurement can be saved into the calibration matrix $\boldsymbol{C}$ with dimensions $M_r \times N$, where N is the number of samples in the azimuth plane where the calibration measurement has been taken. In other words, the generic element of the matrix c_{kj} is a complex value that describes the collected reference measurement result at the end of the pre-processing chain — see Fig. 1 — for the angular position ϑ_j and for the k-th channel.

More formally, the measurement result for an unknown direction can be saved in the vector $\boldsymbol{a}$, which is a column vector with dimension M_r. Then, the cross-correlation between measurement and calibration results is given by

$$\boldsymbol{v}(\vartheta) = \frac{\left| \boldsymbol{C}^H(\vartheta) \cdot \boldsymbol{a} \right|}{\| \boldsymbol{C}(\vartheta) \| \| \boldsymbol{a} \|}, \tag{2}$$

where the symbol $(\cdot)^H$ denotes the complex conjugate (Hermitian) matrix. The dimension of the column vector $\boldsymbol{v}$ is N.

Finally, the estimated DoA is given by

$$\vartheta_{est} = \arg \max_{\vartheta} \boldsymbol{v}(\vartheta), \tag{3}$$

where the function $\arg \max$ gives the angular position ϑ_{est} at which the cross-correlation reaches the maximum.

B. Discrete Fourier Transform Approach

With this simple implementation of the DML procedure presented above it is possible to estimate the position of the target only at the very same points in azimuth, where the calibration results have been collected [21]. Hence, for this basic approach — without any additional processing step — increasing the number of measurement points during the calibration is beneficial to the purpose of the DoA estimation.

However, for many practical applications, and in particular for the mass-production of mm-wave radar sensors, collecting a large number of measurement points might cause a significant increase in the cost and time dedicated to the calibration of a single sensor. This problem will be become even more clear to the reader after the detailed explanation of the calibration procedure that will be presented in Section V. Moreover, typically a large calibration matrix with a sufficient number of measurement points should be saved and then handled by the signal processing unit of the radar system, for example as a lookup table, and this makes the computational effort of the angle estimation larger. Hence, to reduce the calibration effort a second approach is here introduced, which exploits the Fourier transform properties.

This method becomes quite easy to follow by considering a uniform linear array (ULA) as receiving element. In particular, the similarity to the well-known frequency domain analysis of time signals must be recalled for easily understanding the beamforming and DoA estimation problems. Indeed, it is possible to say that the ULA collects the spatial samples of a certain distribution, whose Fourier transform — in this case calculated by means of a DFT — gives the receiving array beam pattern [22].

More formally, the spectrum, i.e., the vector $\boldsymbol{v}(\vartheta)$, can be obtained by collecting the elements relative to the angle ϑ_n

$$v_n = \sum_{k=0}^{M_r-1} a_k \cdot \mathrm{e}^{-\mathrm{j}2\pi \frac{n}{M_r}k}\,, \tag{4}$$

with

$$\vartheta_n \in \arcsin\left[-\frac{1}{2}\frac{\lambda_0}{\Delta x}, \frac{1}{2}\frac{\lambda_0}{\Delta x}\right]\,, \tag{5}$$

where Δx is the constant spacing between adjacent antenna elements in the ULA. The spatial samples a_k contained in the measurement vector $\boldsymbol{a}$ are described by the index k, which in turn represents the k-th receiving channel. The index n indicates the spacing of the frequency vector $\boldsymbol{v}$. The boundaries of (5) are strictly related to the angular range where the DoA estimation can be successfully performed without experiencing any ambiguity. This point will be further discussed in Section IV. Finally, it is also important to remark that in v_n there is no linear dependence on the angle ϑ, but on $\sin\vartheta$, similarly to (1).

Calculating the DFT of the measurement vector $\boldsymbol{a}$ is thus sufficient to solve the DoA estimation problem. Usually, the Fourier transform is calculated with a reasonable zero-padding which results in a smoother-looking spectrum. The typical reciprocal property of the Fourier transform applies also here, so that a wide receiving array generates a beam pattern with a narrow main beam, and vice versa. The estimated DoA ϑ_{est} corresponds to the maximum of the DFT, which gives the position of the main beam in the calculated beam pattern.

Like the previous approach, a calibration is required for the DFT method, too. The non-ideal antenna system must be indeed characterized in order to correctly calculate the DFT, and thus the beam pattern. In particular, the fundamental assumption for using the DFT is that, as reported in (1), for the angular direction of $0°$ the associated value in the steering vector should be 1 for all the receiving channels. Any deviation from the ideal $0°$-value must be compensated.

To summarize, before calculating the DFT, the measurement results must be corrected with the values collected during the calibration for the purpose of obtaining the correct beam pattern.

IV. Assessment Criteria

The angular resolution is a fundamental assessment criterion for DoA estimation problems, in particular to understand whether the antenna system is able to identify two closely spaced targets. From the antenna array theory it is well known that the resolution properties are directly related to the array aperture. A unique widely accepted definition of angular resolution is not available in the literature, however, the Rayleigh criterion has often been used as an important reference metric [1]. The Rayleigh criterion relates the angular resolution $\Delta\vartheta$ in degree to the array (virtual) aperture L as follows

$$\Delta\vartheta = \frac{180°}{\pi}1.22\frac{\lambda_0}{L}\,. \tag{6}$$

Thus, as expected also from the properties of the Fourier transform mentioned in the previous section, the larger the aperture L, the better the resolution. Alternatively, the angular resolution of an antenna system can also be defined as a 3-dB beamwidth or half power beamwidth. The latter will be used in the experimental part of this tutorial as separation criterion to identify two targets.

An unambiguous estimation of the angular position of the target is another fundamental requirement for successfully solving a DoA estimation problem. In this case, the term unambiguity describes the ability of the radar antenna system to uniquely distinguish the DoA of the signal reflected back by the target. This phenomenon comes directly from the well-established concept of grating lobes, which has been nicely explained for example in [23], [24]. Indeed, a grating lobe in the receiving array beam pattern causes an ambiguity in the angular estimation.

This concept has been formally described in [25], where it is possible to find the definition of the ambiguity function $\chi(\vartheta_i, \vartheta_j)$, here recalled for the sake of completeness:

$$\chi(\vartheta_i, \vartheta_j) = \frac{\left|\boldsymbol{y}^H(\vartheta_i)\cdot\boldsymbol{y}(\vartheta_j)\right|}{\parallel\boldsymbol{y}(\vartheta_i)\parallel\parallel\boldsymbol{y}(\vartheta_j)\parallel}\,. \tag{7}$$

It is the autocorrelation of the receiving array steering vector calculated at the positions ϑ_i and ϑ_j, respectively. An ambiguity occurs when it is not possible to distinguish between the directions ϑ_i and ϑ_j. The autocorrelation should indeed return the maximum value of 1 only if $\vartheta_i = \vartheta_j$, and ideally 0 in all the other cases.

Usually, the ambiguity function can be plotted as a three-dimensional plot, where the coordinates x and y describe the angles ϑ_i and ϑ_j, while the z-coordinate depicts the magnitude of the function [26], which is always bounded between 0 and 1.

A simple example of the ambiguity function plot can be seen in Fig. 3. The results refer to an ULA of isotropic radiators with six elements spaced λ_0 apart. The highest value of the autocorrelation has been achieved not only along the main diagonal, where $\vartheta_i=\vartheta_j$, but also for some other angular directions, leading thus to ambiguities. The white box at the center of the plot highlights the area where no ambiguities occur. As known from the array theory, to avoid ambiguities in the estimation of the direction ϑ the following equation must be fulfilled [24]:

$$-\pi \leq 2\pi\frac{\Delta x}{\lambda_0}\sin\vartheta < \pi\,. \tag{8}$$

In principle, if the field of view (FoV) of the radar is confined to the ambiguity-free region, then it is ideally possible to estimate correctly the direction of the target. On the other hand, if the FoV is larger than the ambiguity-free region, then it is possible that some measurements can lead to a wrong DoA estimation.

Avoiding grating lobes is a necessary, but not a sufficient condition for estimating the DoA of a target. For practical applications it is also important to avoid a high sidelobe level. Indeed, high sidelobes could cover for example some weaker targets present in the same range-velocity cell, making thus their correct estimation difficult. High sidelobes can also be
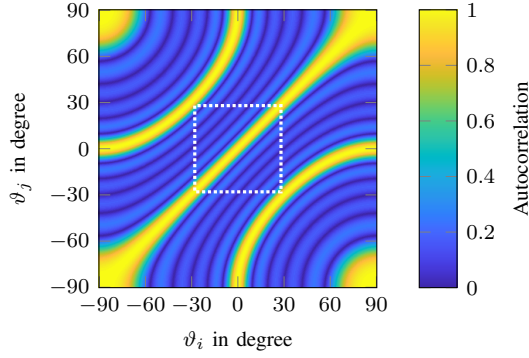
Fig. 3. Plot of the ambiguity function for an ideal six-element uniform linear array with a spacing equal to λ_0 between the elements. The dotted white area describes the ambiguity-free region where no ambiguities occur.
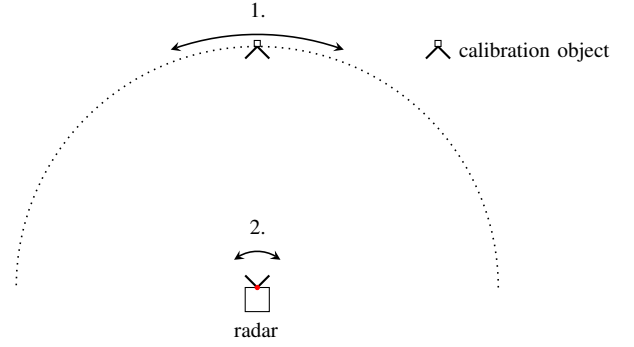

Fig. 4. Possible calibration setup. Either the calibration object is rotated around the radar (1.) or the radar is rotated and the calibration object is located at fixed location (2.).

called *quasi*-ambiguities. Typically, it is possible to adapt the definition of ambiguity-free region to take the quasi-ambiguities also into account [27]. For example, a threshold for an acceptable sidelobe level can be defined, according to the specific application, and then the ambiguity-free region is the area where the ambiguity function $\chi(\vartheta_i, \vartheta_j)$ reaches values below that threshold.

V. CALIBRATION

As already briefly mentioned in Section III, due to differences in the transmission line lengths within the radar systems, manufacturing uncertainties, variances in RF components, different power distribution on the transmit channels, there are amplitude and phase variations between the different transmit-receive channels. These effects result in a deviation from the ideal signal model in (1), described in Section III. The signal model in (1) can be adapted to a more realistic one, which is described by

$$
\boldsymbol{y}(\vartheta) = \begin{bmatrix} A_1(\vartheta)\mathrm{e}^{\mathrm{j}\left(2\pi \frac{x_1}{\lambda_0}\sin\vartheta + \psi_1\right)} \\ \vdots \\ A_{Mr}(\vartheta)\mathrm{e}^{\mathrm{j}\left(2\pi \frac{x_{Mr}}{\lambda_0}\sin\vartheta + \psi_{Mr}\right)} \end{bmatrix}, \qquad (9)
$$

with the phase offset ψ_k and the amplitude A_k for the virtual channel k. Both the amplitude term and the phase are angle dependent. The amplitude term can be neglected if there are no large differences in the amplitude with respect to the incident wave angle. This is usually fulfilled if the antenna is not focusing in the radiation plane — exemplary in the presence of a focusing lens — where the DoA estimation is performed. In the following, the amplitude is neglected.

For the calibration, let us assume a point-like target in the far-field of the antenna array with a known azimuth angle $\vartheta = \vartheta_0$. For a plane wave impinging the antenna array the phase at the receive antenna is described by the exponential term in the signal model of (9). By applying an angle dependent calibration measurement the phase term $\psi(\vartheta) = 2\pi \frac{x_k}{\lambda_0}\sin\vartheta + \psi_k$ can be determined. This can be achieved by a calibration measurement as a function of the azimuth angle ϑ, see Fig. 4.

There are basically two calibration setups:

- **Rotating calibration object**: The radar stays fixed and the calibration object is rotated around the phase center of the radar antenna. This is the most intuitive approach but requires a very accurate positioning system with a large size, which is difficult to realize in practice.
- **Rotating radar**: The same result can be achieved by rotating the radar around its antenna phase center point. This is approximated by a rotation around the center of the antenna frontend. This second approach is more accurate and realizable in practice as it can be done using a stepper motor rotating the radar. Thus, this case is considered in this paper.

As the calibration is conducted for discrete angular step sizes, this results in the matrix C and can be directly applied to the DML of (2). Furthermore, the non-idealities of the antenna array and the phase offsets are included within the calibration measurement.

By only considering the phase of the calibration measurement with respect to the first antenna element, this results in the phase progression curves, see Fig. 6. They behave according to the exponential part of the signal model in (9), which are straight lines if visualized as a function of $\sin\vartheta$.

In the following some key aspects to perform a reliable calibration are discussed.

A. Measurement System

An experimental 77 GHz MIMO radar sensor [11] is used to illustrate the different calibration effects and the measurement examples. The time domain data are directly sampled with a sampling frequency of 20 MHz and saved for a detailed signal processing later on. The bandwidth is set to 2 GHz resulting in a range resolution of 7.5 cm. Four transmitters and eight receivers form a uniform linear array with a $\frac{\lambda_0}{2}$-spacing. The virtual aperture has a length of 15.5 λ_0 and with (6) this leads to an angular resolution of 4.5°. Each single physical antenna element, namely the transmitters and receivers, is an eight-element series-fed patch antenna array using the substrate RO3003. To permit the easy replacing of different antenna frontends, the antenna structure is connected to a waveguide transition simply allowing the use of different antenna setups as shown in Fig. 5. To cover a wide angular range in azimuth,
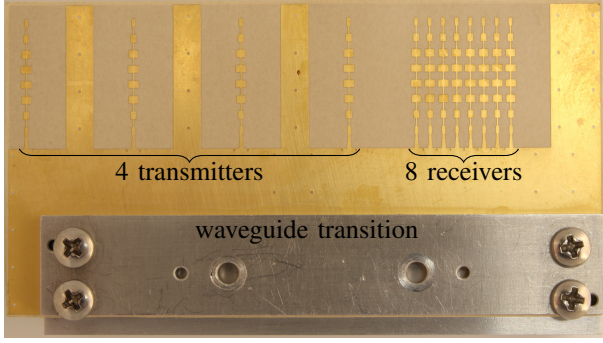
Fig. 5. Picture of the antenna frontend with the four transmitters and eight receivers forming a uniform linear virtual array with a $\frac{\lambda_0}{2}$-spacing between adjacent elements.

the antenna array is focused only in the E-plane and has a single patch characteristic in the H-plane. The calibration as well as the measurement examples are carried out in an anechoic chamber.

B. Influence of the SNR

In the following, the influence of the signal-to-noise ratio (SNR) on the calibration is discussed. The SNR in a measurement is estimated using the mean of all samples not classified as a target by the CFAR and the power level of the current considered target. In Fig. 6, the phase progression over the calibration angles is shown. The used calibration objects are corner reflectors, which differ in their radar cross-section (RCS). For Fig. 6 (a), a corner reflector with an RCS of $6.7\,\mathrm{dBsm}$ is used. This results in a measured SNR value of $32\,\mathrm{dB}$, which is obtained by non-coherent integration of the receive channels. As the value for the SNR is high, the phase curve is smooth and shows a linear trend over a wide angular range. The phase curve is more noisy for large angles, which results from the choice of the antenna element. For the used antenna element, the considered angular range can be confined to $\arcsin(\pm 0.9) \approx \pm 64°$, which is the linear region in Fig. 6 (a).

In contrast, Fig. 6 (b) shows the same phase plot for a corner reflector with an RCS of $-16.4\,\mathrm{dBsm}$ and an SNR value of $11\,\mathrm{dB}$. The reduced SNR leads to the phase plot becoming less smooth and to a smaller angular range, where reliable results can be acquired.

C. Choice of Calibration Objects

There are several calibration objects, which might be used for the setup in Fig. 4. Commonly used calibration objects are corner reflectors, spheres, and cylinders. They are usually fabricated from well-reflecting metals. These objects are most suitable as their radar cross-section, which describes the amount of reflected power, can be analytically described. Additionally, their RCS is very constant for a large angular range.

In the following, only the sphere is compared to the corner reflector. Considering a sphere and assuming that the sphere diameter D is much larger than the wavelength λ_0, its RCS is
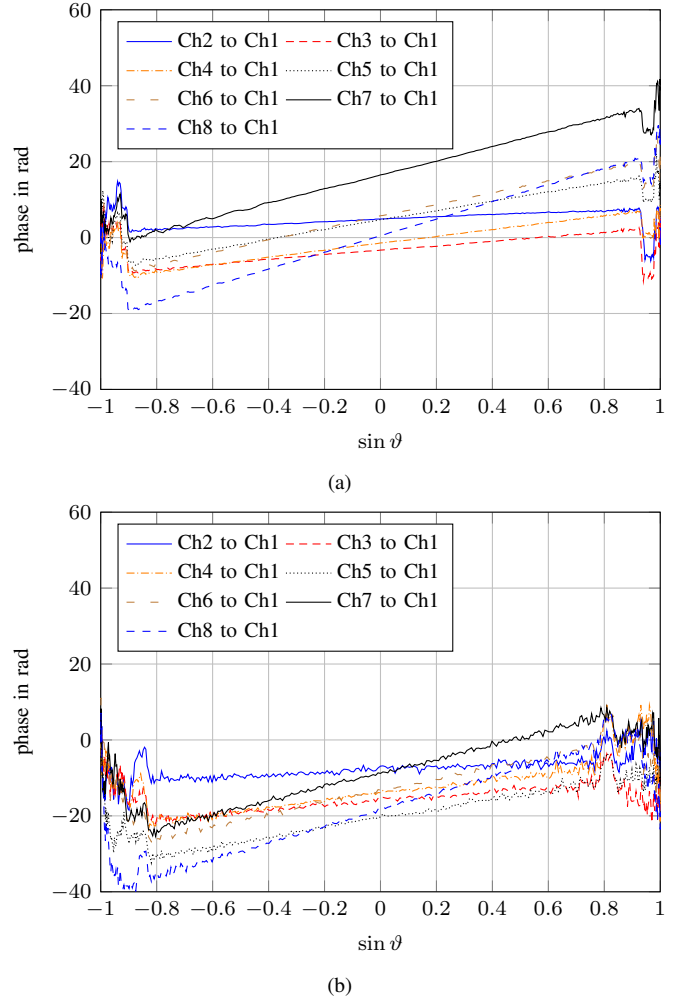

(a)

(b)

Fig. 6. Measurement of the phase progression over the calibration angle for some receive channels relative to the first receive channel. In (a), a high SNR of 32 dB leads to a smooth line for a wide angular range, in (b), a low SNR of 11 dB results in a noisy phase relation and a smaller angular range, where reliable results can be obtained.

the projection of its cross sectional area. In contrast, the RCS of the corner reflector can be described by

$$\sigma_{\mathrm{corner}} = \frac{4\pi}{3}\frac{\left(\frac{a}{\sqrt{2}}\right)^4}{\lambda_0^2},\tag{10}$$

with the outer edge length a. For an exemplary RCS=$0.1\,\mathrm{m}^2$, at $77\,\mathrm{GHz}$, the corner reflector has an outer edge length $a=3.47\,\mathrm{cm}$, whereas a sphere requires a diameter $D=25\,\mathrm{cm}$. The RCS of the corner is frequency dependent and increases with frequency.

In order to conduct a reliable calibration, it is reasonable to place the calibration object in the far-field of the antenna. Additionally, the antenna array should also be in the far-field of the calibration object. Only for these cases plane waves can be assumed and (9) is fulfilled. The far-field distance R can be defined according to [28] by

$$R > 2\frac{L^2}{\lambda_0}.\tag{11}$$

The size L is the largest value between the antenna array size and the size of the calibration object.

In practice, corner reflectors are mostly used as a calibration object in the mm-wave range as it is easier to fulfill the far-field condition in (11). For the exemplary corner reflector with the edge length $a=3.47$ cm and the corresponding sphere with the diameter $D=25$ cm, the far-field condition is fulfilled at 62 cm for the corner reflector and at 32.7 m for the sphere, which is difficult to realize with sufficient SNR, see Section V-B.

D. Limited Number of Angular Steps: A Faster Calibration

The DML estimation can only be applied to discrete azimuth angles for which a calibration exists, cf. Section III. The reasonable number of steps is determined by the resolution of the array given by (6) and the possible ambiguity-free region defined by (8). To allow a precise DoA estimation, the step size is set to $0.5°$. The ULA spacing is $\frac{\lambda_0}{2}$ which results in an ambiguity-free region of $\pm90°$. As the antenna consists of single elements, their radiation pattern must also be taken into account. As mentioned for the SNR considerations shown in Fig. 6 (a), the phase trend is linear in the domain of roughly $\sin(\vartheta) \in [-0.9, 0.9]$ leading to a DoA range of $\pm64°$. Together with the small angular increment this would result in 257 different calibration measurements to determine the steering matrix C for the DML estimation.

In order to reduce the number of required measurement points for the steering matrix C, the key idea is to determine the phase offsets ψ_k of (9) for each single channel and to compensate them. This allows to create the steering matrix Y based on model (1) for a single steering vector without phase deviation. In contrast to the measured matrix C, the created ideal steering matrix Y does not contain any noise and, therefore, leads to a smoother DoA result. In addition, the angular step size can be chosen as small as desired without increasing the measurement effort. Moreover, the removal of the phase offsets is for the application of the Fourier transform based DoA estimation also mandatory as mentioned in Section III.

In theory only a single calibration measurement for a target at $0°$ would be sufficient for the determination of the phase offsets ψ_k. As it is affected by noise, an averaging with several measurements should be considered. Instead of repeating the evaluation of a target under $0°$, a certain angular range is considered. The phase difference $\psi_{k,1}(\vartheta=0°)$ for each channel with respect to the reference channel, e.g., the first one, is then determined by linear regression. The influence of different calibration ranges is depicted in Fig. 7. The overall phase trend is ideally approximated with a wide angular range (⋯⋯⋯), but also a reduced range (‑‑‑‑) already leads to a good approximation. It must be ensured that the phase trend is a straight line and no phase jumps occur. Therefore, the step size for this smaller calibration domain is defined so that the maximum relative phase progression between two calibration steps is much smaller than $\pm180°$ to take phase noise into account. A step size of $0.5°$ leads to a phase progression
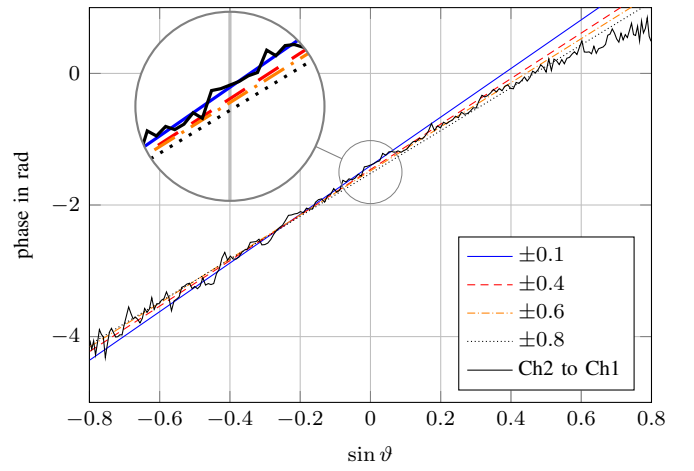

Fig. 7. Instead of measuring the whole angular range (——), smaller ranges are used for the linear regression and compared. The phase value at $0°$ is the phase difference $\Delta\psi_{2,1}(\vartheta=0°)$ between the second and the reference channel.
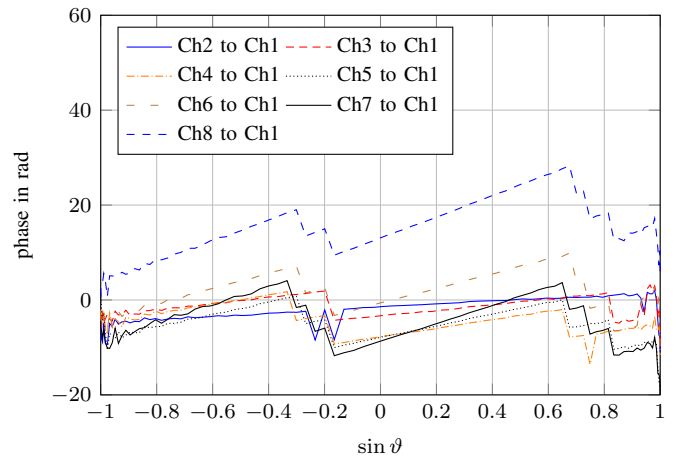

Fig. 8. Calibration with a too large step size of $2°$ leading to phase jumps preventing a reliable linear regression.

between two calibration angles of

$$\Delta\psi_{\max} = 360°\frac{L}{\lambda_0}(\sin 0.5° - \sin 0°) \approx \pm48.7° \qquad (12)$$

for the maximum progression between the first and last virtual channel. For an insufficient calibration step size of $2°$ the maximum phase progression is $\pm194.7°$ leading to phase jumps as can be seen in Fig. 8.

With the determined phase differences $\psi_{k,1}(\vartheta=0°)$ each single channel is corrected in time or frequency domain with

$$\tilde{s}_k = s_k e^{-j\Delta\psi_{k,1}(\vartheta=0°)}. \qquad (13)$$

After calibration, the Fourier transform based DoA is possible as well as the creation of the steering matrix Y, which is later referenced as *ML ideal*.

For a non-ULA array, the DML approach is the easiest choice, as the exact element position is not required. In case of the Fourier transform, either the Fourier transform must be adapted to operate with non-equidistant samples or the missing

element positions with respect to the ULA should be assumed to be zero.

VI. Measurement Examples for DoA Estimation

Two measurement scenarios are presented to highlight different aspects of the DoA estimation. For a single target scenario the influence of the SNR in the calibration on the DoA estimation is shown. In the case of two close targets the three different angle estimation approaches are compared.

A. Single Target Scenario: Influence of the SNR in Calibration

The DoA estimation for a single corner reflector under $20°$ is shown in Fig. 9. With the DML estimation (——) the expected DoA is extracted. For angles larger than $|\vartheta|>64°$ the DoA estimation starts degrading. This behavior is expected as the phase trend in Fig. 6 (a) is stable for the same angular domain. This is the limitation of the single antenna element of the evaluated array. The sidelobe level is as expected at approximately $-13\,\mathrm{dB}$ as no window is applied, which coincides with the theory.

The same DoA estimation is once again performed with the calibration data with less SNR of Fig. 6 (b). Although the DoA can be extracted, the resulting angular spectrum is noisy (– – – –). The loss in SNR should be avoided as additional possible weak targets in the same range-velocity cell could not be detected.

The phase trend is interpolated, and the time domain data is calibrated to allow the application of the ideal steering matrix $\boldsymbol{Y}$. With this matrix the DML estimation is once again performed (– – – –). The resulting angular spectrum has roughly the same shape as the DML approach based on the measured steering matrix, although it is smoothed and has lower sidelobes.

B. Two Close Targets: Performance Comparison

Two corner reflectors of equal size are placed in the same radial distance with a separation of $5°$, which is larger than
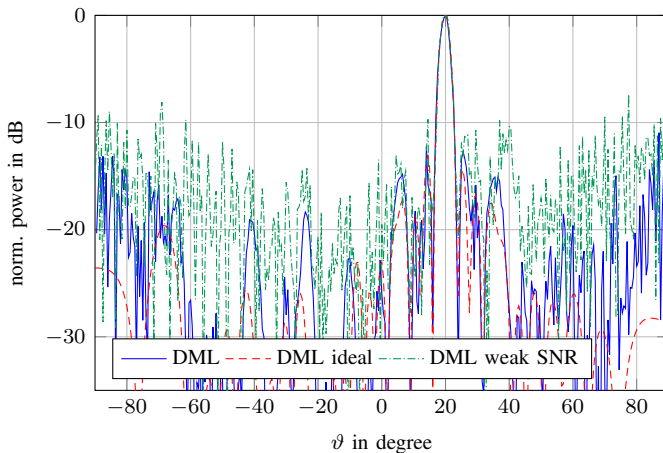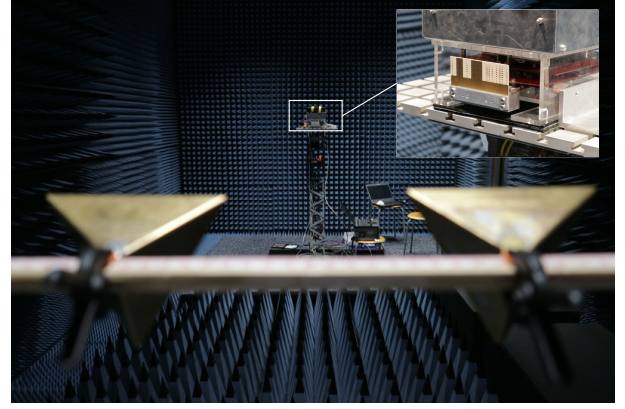

Fig. 10. Measurement setup showing two close corner reflectors with the same radar cross-section. The experimental radar sensor is mounted on a rotary stand visible in the background and shown as an insert.

the theoretical angular resolution of $4.5°$. This measurement setup and the experimental radar sensor mounted on a rotary stand is shown in Fig. 10. The insert is a close-up of the radar sensor with the antenna frontend. The DoA estimation is performed without knowledge or determination of the number of presented targets. Thus, the three different DoA algorithms are applied without any modification and the results are depicted in Fig. 11 to show that close targets can be distinguished.

The DoA based on the measured steering vector (——) shows once again at the edge of the evaluable range the limitation of the antenna elements. The drop in amplitude between the two targets is much larger than $3\,\mathrm{dB}$, which is considered as the separation criterion.

The exploitation of the idealized steering vector (– – – –) has — as in the single target case — less ripples compared to the normal DML approach. The steering entries for the edge of the evaluable range are calculated based upon (1), hence they show no artifacts.

The time domain data is calibrated, and the Fourier transform using a zero-padding to 256 values is applied for DoA estimation (– – – –). This approach yields the same result as the idealized steering vector (– – – –). The reason is, that the Fourier transform is the cross-correlation of the measured steering vector and the complex sinusoidal ideal steering matrix similar to the DML approach.

VII. Conclusions

A practical and straightforward tutorial for DoA estimation with state-of-the-art mm-wave radars, supported by measurements on the basis of a $77\,\mathrm{GHz}$ MIMO radar sensor is presented. For DoA estimation, the sensor calibration is a key task, and a step by step description is provided. Different aspects influencing the quality of the calibration and the reliability of two basic DoA estimation techniques, the DML and the DFT approach, are discussed. Especially the effect of the SNR and the direct related choice of a proper calibration object on the estimation is shown. Measurements with an array with a theoretical angular resolution of $4.5°$ are performed. For a scenario with two targets in the same range-velocity bin separated by only $5°$, the measurement results show that the
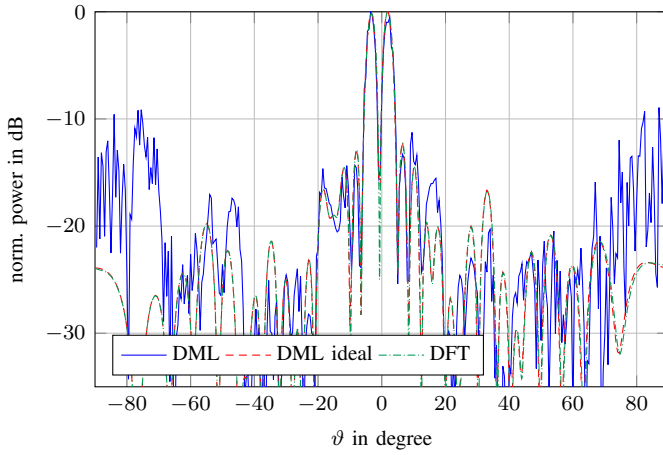

Fig. 9. Measurement of a single target with the measured steering matrix (——), the idealized matrix (– – – –), and the steering matrix obtained of a weak SNR target (– · – · –).

Fig. 11. Measurement of two close targets with the measured steering matrix (——), the idealized matrix (– – – –), and the Fourier transform (–·–·–).

targets can clearly be distinguished and this verifies the here presented procedure.

This paper gave a practical overview of the DoA estimation with mm-wave radars. Further readings about additional DoA estimation techniques can be found in [13], [29] such as the Bartlett beamformer maximizing the power of the direction of arrival, Capon beamformer minimizing the power contribution by noise, or subspace-based methods such as multiple signal classification (MUSIC). The here discussed ambiguity function as an assessment criterion has been introduced for single-target scenarios. In order to extend the ambiguity function towards higher orders the reader can refer to [30]. Using time-division multiplexing (TDM) to achieve orthogonal signals for MIMO radars, special care must be taken in the case of moving targets, which lead to phase errors and can result in inaccurate or unusable angular estimation. Either overlapping elements [31] or an adaption of the DFT [32] can be used to overcome this issue. Last but not least, sparse antennas can be employed to enhance the angular resolution while maintaining a limited number of transmitters and receivers. Using compressed sensing, the missing antenna elements can be reconstructed in order to mitigate the high side lobes [33].

VIII. ACKNOWLEDGMENT

IX. AUTHOR INFORMATION

Claudia Vasanelli (claudia.vasanelli@alumni.uni-ulm.de) received her Ph.D. degree from Ulm University, Ulm, Germany, in 2019. Her research interests focus on mm-wave antenna systems, in particular for automotive radar applications.

Fabian Roos (roos@ieee.org) is currently pursuing his Ph.D degree at Ulm University, Ulm, Germany. His research interest includes automotive radar and environmental perception with a focus on adaptivity for chirp-sequence modulated automotive radar sensors.

André Dürr (andre.duerr@uni-ulm.de) is currently working towards his Ph.D degree at Ulm University, Ulm, Germany. His research interests are high-resolution imaging radars in the upper millimeter-wave range, performance degradation of non-coherent multi-channel radar systems, and their synchronization.

Johannes Schlichenmaier (schlichenmaier@ieee.org) is working towards his Ph.D. degree at Ulm University, Ulm, Germany. His research interests include advanced signal processing for cooperative radar networks as well as detection and estimation of extended radar objects in automotive scenarios.

Philipp Hügler (paul.huegler@uni-ulm.de) is currently pursuing the Ph.D. degree at Ulm University, Ulm, Germany. His research focuses on imaging radar front-ends for small UAVs.

Benedikt Meinecke (benedikt.meinecke@uni-ulm.de) is working towards his Ph.D. at Ulm University, Ulm, Germany. His research focuses on system concepts for multistatic coherent radar networks and the accompanying signal processing.

Maximilian Steiner (Maximilian.Steiner@uni-ulm.de) is currently pursuing the degree Ph.D. in electrical engineering at Ulm University, Ulm, Germany. His research interests include system concepts for radar sensor networks in automotive and robotic scenarios as well as the accompanying signal processing.

Christian Waldschmidt (christian.waldschmidt@uni-ulm.de) was appointed in 2013 director of the Institute of Microwave Engineering at Ulm University, Ulm, Germany, as a full professor. His research topics focus on radar, submillimeter-wave engineering, and antennas.

X. EXEMPLARY DOA ESTIMATION: DML APPROACH

This example requires the measured calibration matrix C. A *MATLAB* syntax is chosen to illustrate the required processing steps.

```
% input variables
% a: the measurement steering vector is a complex column
     vector
% C: the calibration matrix with each column representing a
     measurement steering vector

% calculate the cross−correlation of (2)
% −> the Hermitian operator is realized with a complex
     conjugation conj and the transposition .'
% −> the normalization is done with the Euclidean norm by
     summing the squared values and taking the root of it
% −> C(:) converts the matrix to a vector, hence, a sum of
     the vector is required and not a double sum
A = conj(C).' * a / ( sqrt(sum(abs(a).^2)) * sqrt(sum(abs(C
    (:)).^2)) );

% −> convert the spectrum to a logarithmic scale
A = 10*log10( abs(A).^2 );

% the x axis is dependent on the measured angular steps, in
     this example equal calibration steps
% from [−90,90] degree have been captured
plot(linspace(−90,90,numel(A)), A)
```

XI. EXEMPLARY DOA ESTIMATION: FFT APPROACH

This example expects a uniform linear array, because then the DFT equation (4) can be simplified to a Fast Fourier Transform. Additionally, the calibration — as mentioned in

(13) — has to be applied to ensure that a target at 0° leads to equal phases at all channels. A *MATLAB* syntax is chosen to illustrate the required processing steps.

```
% input variables
% a: the calibrated measurement steering vector is a
    complex column vector

% calculate the Fast Fourier Transform
% -> the input vector has 32 entries, for a smoother
    spectrum use a zero-padding to 256 values
% -> normalize the spectrum with the number of input
    samples
% -> this is (4) written with the fft function
A = fft(a, 256) ./ numel(a);

% -> convert the spectrum to a logarithmic scale
A = 10*log10( abs(A).^2 );

% as stated in (5), the spectrum is linear in sin(theta),
    hence create the frequency vector with arcussin
% -> scale it linearly and then apply the arcussin
f = asin( linspace( -0.5 * lambda_0 / delta_x, 0.5 *
    lambda_0 / delta_x, 256 ) );

% some programs output the spectrum from [0,fs] and not
    from [-fs/2,fs/2], with fs being the sampling frequency
% -> the fftshift shifts the spectrum to be in [-theta_min,
    theta_max]
% -> convert the angle from radians to degree scaling
plot(rad2deg(f), fftshift(A))
```

XII. EXEMPLARY DoA ESTIMATION: DFT APPROACH

In contrast to the FFT approach, the DFT version can be applied to a non uniform linear array as well, although this example expects the ULA. Additionally, the calibration — as mentioned in (13) — has to be applied to ensure that a target at 0° leads to equal phases at all channels. A *MATLAB* syntax is chosen to illustrate the required processing steps. The following example is a practical implementation of (4).

```
% input variables
% a: the calibrated measurement steering vector is a
    complex column vector

% the input measurement steering vector is zero-padded to
    this length
L = 256;

% preallocate the resulting frequency vector
v_n = zeros(L, 1);

% zero-padd the measurement steering vector to the same
    length
a_zp = [a; zeros(L-numel(a),1)];

% calculate the DFT (4) by hand
% -> the measurement steering vector ranges from [0,L-1],
    which is without zero-padding [0,Mr-1]
theta = 0:L-1;
% -> this for loop calculates the whole frequency vector in
    contrast to (4) which only calculates a single
    frequency spectrum value
for k = 1:numel(theta)
    % -> the kthe frequency spectrum value in (4) consists
        of a sum, which is here realized with a vector
        product of a row and a column vector to be more
        efficient
    % -> the current frequency is theta(k) which is in (4)
        the n
    % -> the division by Mr in (4) is written as numel(a_zp
        )
    % -> in the sum, k is increased vom [0,Mr-1], which is
        here [0,L-1] due to the zero-padding. the column
        vector for the vector product is created with the
        colon : operator and a transposition .'
    v_n(k) = a_zp.' * exp(-1i*2*pi * theta(k) / numel(a_zp)
        * (0:numel(a_zp)-1)).';
end
```

```
% -> convert the spectrum to a logarithmic scale
v_n = 10*log10( abs(v_n).^2 );

% as stated in (5), the spectrum is linear in sin(theta),
    hence create the frequency vector with arcussin
% -> scale it linearly and then apply the arcussin
f = asin( linspace( -0.5 * lambda_0 / delta_x, 0.5 *
    lambda_0 / delta_x, L ) );
plot(rad2deg(f), v_n)
```

REFERENCES

[1] J. Hasch, E. Topak, R. Schnabel, T. Zwick, R. Weigel, and C. Waldschmidt, "Millimeter-Wave Technology for Automotive Radar Sensors in the 77 GHz Frequency Band," *IEEE Trans. Microw. Theory Tech.*, vol. 60, no. 3, pp. 845–860, Mar. 2012.

[2] J. Dickmann, N. Appenrodt, J. Klappstein, H.-L. Bloecher, M. Muntzinger, A. Sailer, M. Hahn, and C. Brenk, "Making Bertha See Even More: Radar Contribution," *IEEE Access*, vol. 3, pp. 1233–1247, 2015.

[3] A. Schiessl, S. S. Ahmed, A. Genghammer, and L. Schmidt, "A Technology Demonstrator for a 0.5 m × 0.5 m Fully Electronic Digital Beamforming mm-Wave Imaging System," in *5th European Conf. on Antennas and Propagation (EUCAP)*, April 2011, pp. 2606–2609.

[4] S. Ayhan, M. Pauli, S. Scherr, B. Gottel, A. Bhutani, S. Thomas, T. Jaeschke, J.-M. Panel, F. Vivier, L. Eymard, A. Weill, N. Pohl, and T. Zwick, "Millimeter-Wave Radar Sensor for Snow Height Measurements," *IEEE Trans. Geosci. Remote Sens.*, vol. 55, no. 2, pp. 854–861, Feb. 2017.

[5] W. Menzel, "Millimeter-Wave Radar for Civil Applications," in *7th European Radar Conf.*, Sept. 2010, pp. 89–92.

[6] M. Geiger, M. Hitzler, S. Saulig, J. Iberle, P. Hugler, and C. Waldschmidt, "A 160-GHz Radar With Flexible Antenna Used as a Sniffer Probe," *IEEE Sensors Journal*, vol. 17, no. 16, pp. 5104–5111, Aug. 2017.

[7] A. Ascher, R. Lenz, and S. Heuel, "A novel approach to measure the automotive radar sensor's robustness against interferers in the lab with realistic scenarios," in *19th International Radar Symposium (IRS)*. IEEE, June 2018.

[8] S. B. J. Gowdu, M. Asghar, J. Nagel, M. Rožmann, R. Stephan, and M. A. Hein, "Comparison of real and simulated automotive radar targets measured with a reference radar," in *International Conf. on Electromagnetics in Advanced Applications (ICEAA)*. IEEE, Sept. 2018.

[9] R. Feger, C. Wagner, S. Schuster, S. Scheiblhofer, H. Jäger, and A. Stelzer, "A 77-GHz FMCW MIMO Radar Based on an SiGe Single-Chip Transceiver," *IEEE Trans. Microw. Theory Tech.*, vol. 57, no. 5, pp. 1020–1035, May 2009.

[10] S. Lutz, T. Walter, and R. Weigel, "Lens-based 77 GHz MIMO radar for angular estimation in multitarget environments," *Int. Journal of Microw. Wireless Technologies*, vol. 6, no. 3-4, pp. 397–404, Apr. 2014.

[11] P. Hügler, F. Roos, M. Schartel, M. Geiger, and C. Waldschmidt, "Radar Taking Off: New Capabilities for UAVs," *IEEE Microw. Mag.*, vol. 19, no. 7, pp. 43–53, Nov. 2018.

[12] L. Godara, "Application of antenna arrays to mobile communications. part II. beam-forming and direction-of-arrival considerations," *Proceedings of the IEEE*, vol. 85, no. 8, pp. 1195–1245, 1997.

[13] H. Krim and M. Viberg, "Two Decades of Array Signal Processing Research: The Parametric Approach," *IEEE Signal Process. Mag.*, vol. 13, no. 4, pp. 67–94, July 1996.

[14] V. Winkler, "Range Doppler Detection for automotive FMCW Radars," in *European Radar Conf.*, Oct. 2007, pp. 166–169.

[15] F. J. Harris, "On the Use of Windows for Harmonic Analysis with the Discrete Fourier Transform," *Proc. of the IEEE*, vol. 66, no. 1, pp. 51–83, Jan. 1978.

[16] G. Payá-Vayá and H. Blume, *Towards a Common Software/Hardware Methodology for Future Advanced Driver Assistance Systems*, ser. River Publishers Series in Transport Technology. River Publishers, 2017.

[17] H. Rohling, "Radar CFAR Thresholding in Clutter and Multiple Target Situations," *IEEE Trans. Aerosp. Electron. Syst.*, vol. AES-19, no. 4, pp. 608–621, July 1983.

[18] M. Harter, J. Hildebrandt, A. Ziroff, and T. Zwick, "Self-Calibration of a 3-D-Digital Beamforming Radar System for Automotive Applications With Installation Behind Automotive Covers," *IEEE Trans. Microw. Theory Tech.*, vol. 64, no. 9, pp. 2994–3000, Sept. 2016.

[19] J. Li and P. Stoica, *MIMO Radar Signal Processing*. Wiley-IEEE Press, 2008.

[20] I. Bekkerman and J. Tabrikian, "Target Detection and Localization Using MIMO Radars and Sonars," *IEEE Trans. Signal Process.*, vol. 54, no. 10, pp. 3873–3883, Oct. 2006.

[21] T. E. Tuncer and B. Friedlander, Eds., *Classical and Modern Direction-of-Arrival Estimation*. Elsevier Science, 2009. [Online]. Available: https://www.ebook.de/de/product/15174431/classical_and_modern_direction_of_arrival_estimation.html

[22] D. Brandwood, *Fourier Transforms in Radar and Signal Processing (Artech House Radar Library (Hardcover))*. Artech House Publishers, 2003.

[23] C. A. Balanis, *Antenna Theory: Analysis and Design*, 2nd ed. Wiley, 1996.

[24] H. J. Visser, *Array and Phased Array Antenna Basics*. Wiley, 2005.

[25] M. Eric, A. Zejak, and M. Obradovic, "Ambiguity characterization of arbitrary antenna array: type I ambiguity," in *IEEE 5th Int. Symposium Spread Spectrum Tech. Applications - Proceedings. Spread Technology to Africa*, vol. 2, Sept. 1998, pp. 399–403.

[26] M. C. Sullivan, *Practical Array Processing*. McGraw-Hill Education, 2008.

[27] C. Vasanelli, R. Batra, A. Di Serio, F. Boegelsack, and C. Waldschmidt, "Assessment of a Millimeter-Wave Antenna System for MIMO Radar Applications," *IEEE Antennas Wireless Propag. Letters*, vol. 16, pp. 1261–1264, 2017.

[28] R. C. Johnson, *Antenna Engineering Handbook*, 3rd ed. McGraw-Hill Inc., 1993.

[29] R. Schmidt, "Multiple Emitter Location and Signal Parameter Estimation," *IEEE Trans. Antennas Propag.*, vol. 34, no. 3, pp. 276–280, Mar. 1986.

[30] P. Häcker and B. Yang, "Mixed-Order and Higher-Order Ambiguity Functions," in *IEEE Intelligent Vehicles Symposium (IV)*, Jun. 2011, pp. 752–757.

[31] C. Schmid, R. Feger, C. Pfeffer, and A. Stelzer, "Motion Compensation and Efficient Array Design for TDMA FMCW MIMO Radar Systems," in *6th European Conf. on Antennas and Propagation (EUCAP)*, Mar. 2012, pp. 1746–1750.

[32] J. Bechter, F. Roos, and C. Waldschmidt, "Compensation of Motion-Induced Phase Errors in TDM MIMO Radars," *IEEE Microw. Wireless Compon. Letters*, vol. 27, no. 12, pp. 1164–1166, Dec. 2017.

[33] F. Roos, P. Hügler, L. L. Tovar Torres, C. Knill, J. Schlichenmaier, C. Vasanelli, N. Appenrodt, J. Dickmann, and C. Waldschmidt, "Compressed Sensing based Single Snapshot DoA Estimation for Sparse MIMO Radar Arrays," in *German Microwave Conf. (GeMiC)*, Mar. 2019, pp. 1–4.